EDGE ARTICLE

Orbital energy mismatch engenders high-spin ground states in heterobimetallic complexes†

Scott C. Coste, [ID] [a] Tyler J. Pearson, [ID] [a] Alison B. Altman,[a] Ryan A. Klein, [ID] [a] Brian A. Finney,[b] Michael Y. Hu, [ID] [c] E. Ercan Alp,[c] Bess Vlaisavljevich [ID] [b] and Danna E. Freedman [ID] *[a]

The spin state in heterobimetallic complexes heavily influences both reactivity and magnetism. Exerting control over spin states in main group-based heterobimetallics requires a different approach as the orbital interactions can differ substantially from that of classic coordination complexes. By deliberately engendering an energetic mismatch within the two metals in a bimetallic complex we can mimic the electronic structure of lanthanides. Towards this end, we report a new family of complexes, [^{Ph,Me}TpMSnPh$_3$] where M = Mn (**3**), Fe (**4**), Co (**5**), Ni (**6**), Zn (**7**), featuring unsupported bonding between a transition metal and Sn which represent an unusual high spin electronic structure. Analysis of the frontier orbitals reveal the desired orbital mismatch with Sn 5s/5p primarily interacting with 4s/4p M orbitals yielding localized, non-bonding d orbitals. This approach offers a mechanism to design and control spin states in bimetallic complexes.

Introduction

Synthetic control over spin state in transition metal complexes is crucial for tuning magnetic properties[1] and reactivity.[2–7] An intriguing method for creating high-spin bimetallic complexes is inspired by lanthanide complexes, in which the f orbitals are spatially contracted and thus do not interact with the ligand field. In transition metal complexes we can engineer an energetic mismatch between the frontier orbitals of the ligands and the 3d orbitals of the metal to afford a similar orbital depiction. From a molecular orbital (MO) perspective, poor energetic alignment between ligand donor and metal d orbitals would yield highly localized d orbitals exhibiting minimal interaction with the ligand field. We hypothesize using a heavy main group metal donor, such as Sn, could facilitate this energy mismatch as its electropositivity and larger principal quantum number theoretically render higher energy frontier orbitals.[8] This approach will also provide key insight into the electronic structure of transition metal–Sn complexes which are of interest for cooperative catalysis[9–12] and radical-based transformations.[13–16]
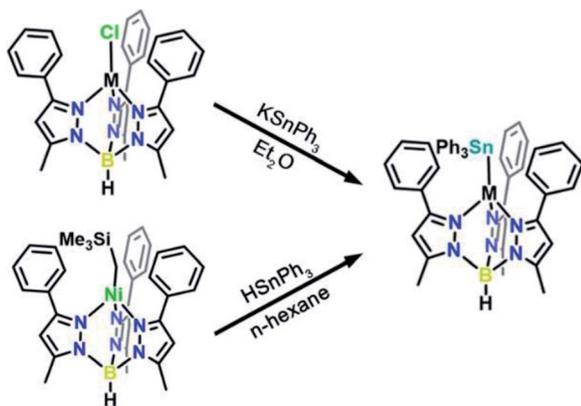
[a]Department of Chemistry, Northwestern University, Evanston, Illinois, 60208, USA. E-mail: danna.freedman@northwestern.edu

[b]Department of Chemistry, University of South Dakota, Vermillion, South Dakota, 57069, USA

[c]Advanced Photon Source, Argonne National Laboratory, Lemont, IL, 60439, USA

Herein, we report an isostructural series of transition metal–Sn complexes, [^{Ph,Me}TpMSnPh$_3$] (^{Ph,Me}Tp$^-$ = hydrotris(3-phenyl-5-methylpyrazolyl)borate; M = Mn (**3**), Fe (**4**), Co (**5**), Ni (**6**), Zn (**7**)), in which high spin ground states are stabilized by an unusual bonding interaction. Using a series of first row transition metals allows us to probe the ligand field from various techniques while controlling metal–metal covalency to understand bonding. Despite a covalent interaction between the Sn and the transition metals, *i.e.* a similar atomic contribution to a bonding MO, Sn minimally interacts with the 3d manifold of the transition metal. This yields highly localized d orbitals on the transition metal exhibiting a weak field electronic structure. We attribute this observation to energetic mismatch between the 5s/5p donor orbitals of Sn and the 3d orbitals of the transition metal.

Results and discussion

We targeted unsupported metal–metal bonds to diminish the impact of ancillary ligands on the electronic structure. A divalent metal (Mn^{2+}, Fe^{2+}, Co^{2+}, Ni^{2+}, Zn^{2+}) is capped with hydrotris(3-phenyl-5-methylpyrazolyl)borate (^{Ph,Me}Tp$^-$) leaving an open axial site for Sn coordination. Reacting this fragment with the organometallic anion, triphenyl stannide (Ph$_3$Sn$^-$), yielded the desired four-coordinate complexes featuring unsupported metal–metal bonds between these transition metals and Sn. We accessed complexes **3–7** *via* two routes as shown in Scheme 1. Compounds **3**, **4**, **5**, and **7** form by metathesis of ^{Ph,Me}TpMCl (M = Mn^{2+}(**1**), Fe^{2+}, Co^{2+}, Zn^{2+}(**2**))[17,18] with KSnPh$_3$ in diethyl ether.[19] To access **6**, we reacted

Scheme 1 Synthetic pathways to **3–7**. M = Mn, Fe, Co, Ni, Zn.

a trimethylsilyl Ni complex with HSnPh₃ in *n*-hexane to eliminate trimethylsilane as **6** was unstable towards metathesis reaction conditions. Further synthetic details are available in the ESI.†

The molecular structures of **3–6** were determined from single crystal X-ray diffraction. The structures (Fig. 1) show that both metals exist in a pseudo-tetrahedral environment connected by an unsupported metal–metal bond. These complexes crystallize isostructurally in $R\bar{3}$, as corroborated by PXRD (Fig. S1†), with the metal–metal bond coinciding with the 3-fold rotation axis. The M–Sn bond distances in complexes **3**, **4**, **5**, **6**, and **7** (2.757(1), 2.698(1), 2.654(1), 2.668(1), and 2.603(1) Å respectively) are similar to or shorter than the sum of their covalent radii suggesting the presence of covalent bonding.[20] Analysis of the bonding *via* Cotton's formal shortness ratio (FSR) yields values of 1.040, 1.018, 1.010, 1.017, and 0.962, respectively.[21,22] The similar values demonstrate that the metal–metal bonds have comparable bond order but that the Zn–Sn bond in **7** is the strongest. The vibrational Raman spectra (Fig. S2†) support this analysis where the metal–metal stretching frequencies of **3–6** are between 170–173 cm⁻¹ but the stretching mode in **7** is 180 cm⁻¹.

We probed the spin ground state in complexes **3–6** using SQUID magnetometry. Variable-temperature dc magnetic susceptibility data (shown in Fig. 2) on polycrystalline samples

of **3**, **4**, **5**, and **6** display room-temperature $\chi_M T$ values of 4.32, 3.58, 2.61, and 1.36 cm³ K mol⁻¹ in accordance with $S = \frac{5}{2}$, $S = 2$, $S = \frac{3}{2}$, and $S = 1$ ground states, respectively. The room-temperature values persist down until ~15 K in **3** and **6** or ~100 K in **4** and **5**, which we attribute to the presence of zero-field splitting, *D*, a parameter for magnetic anisotropy. The high-spin state in the M–Sn bonded complexes here is rare as many such compounds feature low-valent strong-field environments.[23,24] The high-spin nature here provides a unique opportunity to probe the ligand field influence of Sn to assess the metal–metal bonding.

We began our assessment of the ligand field in **3–6** with electronic absorption and ⁵⁷Fe Mössbauer spectroscopy. Diffuse reflectance spectra of **3–6** (Fig. 3) show charge transfers in the UV-visible region and d–d transitions at lower energies. We assign the former as Ph₃Sn → M (M = Mn, Fe, Co, Ni) metal-to-metal charge transfer (MMCT) reflecting the stability of Sn's higher oxidation states. This assignment is supported by the lack of comparable CT bands in the parent chloride compounds and by the similar intensity between the CT (~10³ L mol⁻¹ cm⁻¹) and higher energy d–d transitions.[25,26] The MMCT band red-shifts linearly with increasing transition metal
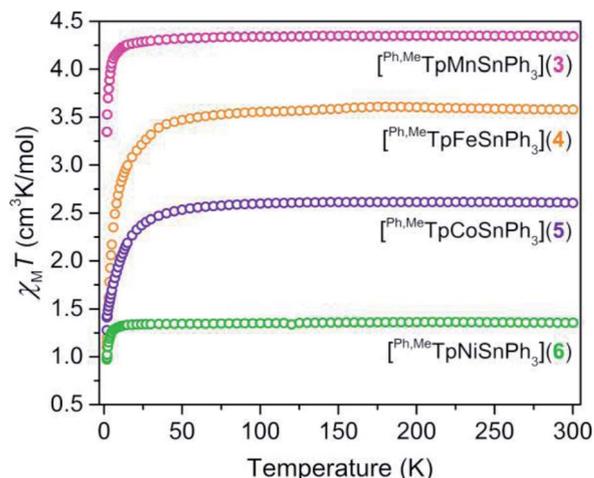

Fig. 2 Temperature dependent magnetic susceptibility of polycrystalline powders of **3–6** collected under an applied field of 0.1 T.
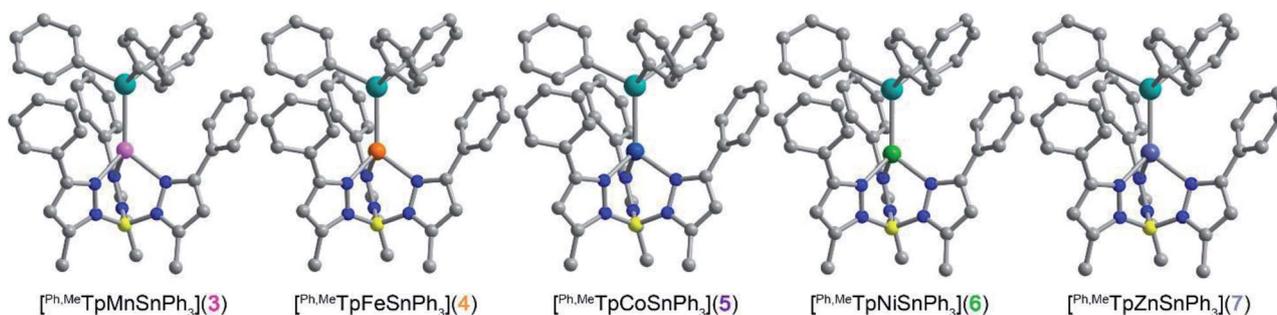

Fig. 1 Molecular structures of the [^{Ph,Me}TpMSnPh₃] series determined by X-ray crystallography where M = Mn (**3**), Fe (**4**), Co (**5**), Ni (**6**), and Zn (**7**). The blue, grey, yellow, turquoise, pink, orange, cobalt blue, green, and purple spheres represent nitrogen, carbon, boron, tin, manganese, iron, cobalt, nickel, and zinc atoms respectively. The hydrogens are omitted for clarity.
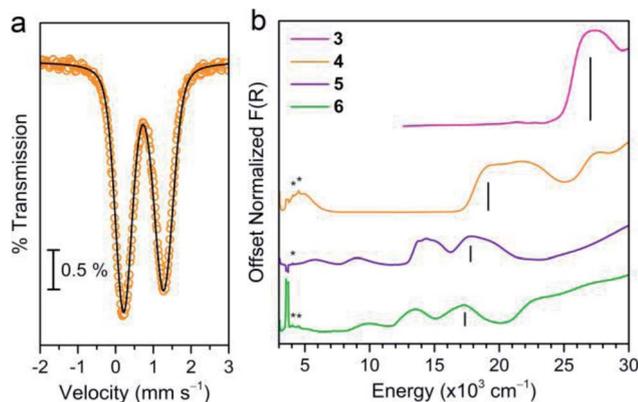
Fig. 3 (a) ^{57}Fe Mössbauer spectra for a powder sample of **4** collected at 80 K. Open circles represent the experimental data, and the black line represents the fit to the spectrum. (b) Diffuse reflectance of **3–6** measured in KBr at room temperature where the black bars mark the MMCTs. The asterisks mark absorbances from the ligand, and the water absorbance at ~3300 cm^{-1} has been manually removed from the data.

electronegativity (Fig. S5†), implying the energetic stabilization of the acceptor d orbitals with increasing electronegativity.[27,28] The d–d transition energies and intensities in **5** and **6** are characteristic of $^4A_2$ and $^3A_2$ ground states, implying the following frontier orbital energy ordering: e(d$_{xz}$, d$_{yz}$) > a$_1$(d$_{z^2}$) > e(d$_{xy}$, d$_{x^2-y^2}$).[29,30,39] The ^{57}Fe Mössbauer spectrum of **4** at 80 K (Fig. 3b) corroborates a similar d orbital ordering where the isomer shift ($\delta = 0.742(1)$ mm s^{-1}) and ΔE_Q values (1.061(3) mm s^{-1}) are similar to other C_{3v}-symmetric ferrous complexes with a ^{5}E ground state (tabulated in Table S7†).[31,32] Importantly, the d–d transition energies of **4–6** are lower than that of structurally similar Tp$^-$ metal halide complexes suggesting a weak ligand field environment. This contrasts with previous studies of Sn ligands, which characterize it as a relatively strong σ-donor.[33–36] This discrepancy prompted us to investigate the degree of Sn character in the 3d-based MOs.

To probe the contribution of Sn towards the d orbitals, we used the zero-field splitting and hyperfine parameters from magnetometry and electron paramagnetic resonance (EPR) spectroscopy. As magnetic anisotropy stems from spin–orbit coupling (SOC), we would expect a high degree of covalency between 3d orbitals and the heavy Sn donor to yield larger axial zero field splitting (D) values compared to lighter ligands with smaller SOC constants.[37] We quantified the magnetic anisotropy in **4–6** using SQUID magnetometry, specifically through variable-field, variable-temperature magnetization data (Fig. S7†); the magnetic properties of **5** were reported previously.[19] Using the program DAVE 2.0,[38] we simulated the magnetization data with the spin Hamiltonian $\hat{H} = g_{iso}\mu_B SH + D[\hat{S}_z^2 - S(S+1)/3] + E(\hat{S}_x^2 - \hat{S}_y^2)$ where g_{iso} is the isotropic g-value, μ_B is the Bohr magneton, S is the spin quantum number, H is the applied magnetic field, D is the axial zero-field splitting parameter, and E is the transverse zero-field splitting parameter. The D values extracted for **4**, **5**, and **6** from the simulations are 12.9(3) cm^{-1} ($E/D = 0.26$), 11.9(1) cm^{-1} ($E/D = 0.06$) and

−3.0(2) cm^{-1} ($E/D = 0$), respectively. These values are both surprisingly small relative to isoelectronic C_{3v} symmetric complexes regardless of donor SOC.[39–45]

The D value and hyperfine analysis of **3** were determined through X-band EPR spectroscopy. A spectrum of a solid state dilution of **3** in **7** (1 : 20 Mn : Zn) is shown in Fig. 4 where Sn hyperfine is prevalent in the intra-Kramers ($M_S = \pm\frac{1}{2}$) transition (inset). We modelled the spectrum using EASYSPIN[46] with the following spin Hamiltonian, $\hat{H} = g_{iso}\mu_B SH + AIS + D[\hat{S}_z^2 - S(S+1)/3]$ where all parameters hold their previous definitions and A is the hyperfine coupling tensor and I is the nuclear spin. The best simulation to the EPR spectrum of **3** at 12 K (shown in Fig. S8†) reveals a D value of 0.1015(6) cm^{-1} at 12 K, which is much smaller in comparison to D values with heavy atom donors such as iodide.[47,48] Remarkably, the D value of **1**, with the notably ionic axial Cl donor to Mn replacing Sn, is almost twice that of **3** corroborating the relatively small D values from magnetometry in **4–6**. The D values reported here broadly suggest there is little SOC contribution from the heavy Sn donor towards magnetic anisotropy.

Analysis of the metal hyperfine parameters in Fig. 4 yields a ^{nat}Sn hyperfine coupling ($I = \frac{1}{2}$ for ^{115}Sn, ^{117}Sn, and ^{119}Sn) of 141(3) MHz and a ^{55}Mn hyperfine coupling ($I = \frac{5}{2}$) of 164(2) MHz. The ^{55}Mn hyperfine coupling parameter is low relative to other Mn^{2+} species, which can be attributed to the presence of covalent bonding based on previous observations.[49] Despite the comparable metal hyperfine magnitude, the ^{nat}Sn hyperfine in **3** is only ~3% as large as Sn-centered radicals, such as Ph$_3$Sn$^•$ (5230 MHz) where the spin density is completely localized at the Sn nucleus.[50] This suggests there is little covalency between the 3d$_{z^2}$ based orbital and the Sn donor orbitals. The foregoing
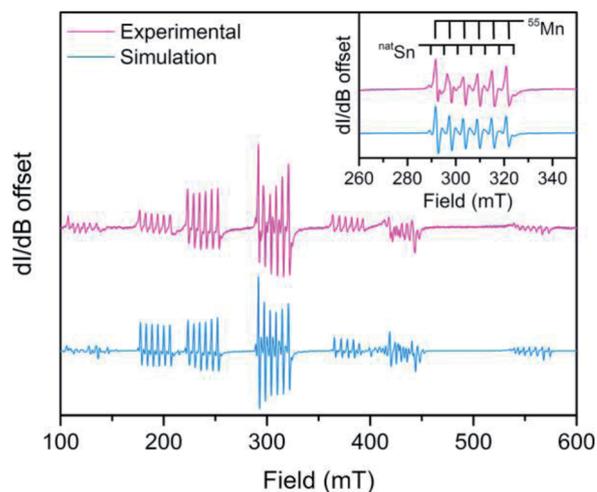

Fig. 4 Overlay of the experimental (pink) cw-EPR spectrum of **3** diluted in a polycrystalline sample of **7** (Mn : Zn 1 : 20) and the simulation (light blue) at room temperature collected at X-band ($\nu = 9.6328$ GHz). Inset: a zoomed image of the intra-Kramers ($M_S = \pm\frac{1}{2}$) transition. The light blue spectrum was simulated using the following parameters: $g_{iso} = 1.9933(2)$, $S = \frac{5}{2}$, $A_{iso}(^{55}Mn, I = \frac{5}{2}) = 164(2)$ MHz, $A_{iso}(^{nat}Sn, I = \frac{1}{2}) = 141(3)$ MHz, $D = 0.0939(4)$ cm^{-1}.

analyses indicate a lack of Sn character in the d-based MOs suggesting an ionic interaction.

To assess the covalency of the metal–metal bonds in **3–7**, we used X-ray spectroscopic techniques to probe the electron distribution about the Sn nucleus. The X-ray absorption near-edge spectra (XANES) at the Sn K-edge are shown in Fig. 5a. The XANES region are similar in **3–7** where the intensities and onset energy overlay well. The onset energy, defined by the energy of the inflection point (better illustrated by plotting the first derivative shown in Fig. S9†), for each compound is 29 201.7 eV. This indicates that the Sn valency does not change between **3–7** within the resolution limit of the Sn K-edge.[51–54]
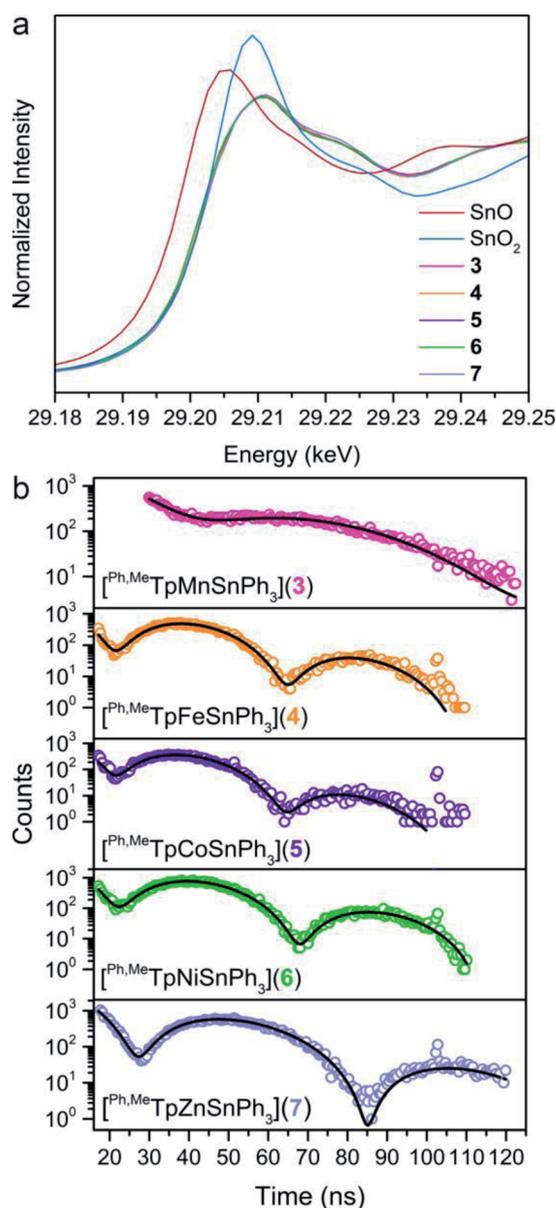

Fig. 5 (a) The XANES spectra at the Sn K-edge for polycrystalline samples of **3–7** (29 200.4 eV for Sn metal reference), including SnO and SnO$_2$ standards, measured at 25 K. (b) ^{119}Sn synchrotron Mössbauer spectra of **3–7** collected at 60 K. Open circles represent the experimental data, and the black lines represent fits to the spectra.

Importantly, the onset energies of **3–7** are between that of the SnO and SnO$_2$ references, 29 200.1 and 29 203.4 eV respectively, alluding to a Sn valency between +2 and +4. Comparison of the onset energy between **3–7** with structurally similar organometallic controls, ∼29 201.1 eV for Ph$_3$SnX (X = SnPh$_3$, Ph, Cl, and F), further corroborates the apparent Sn valency (Fig. S9†). This observation matches the valence trends in ^{119}Sn Mössbauer spectra of transition metal–Sn^{2+} complexes where the isomer shift values are closer to those of Sn^{4+} than Sn^{2+}.[9] We attribute these observations to significant donation of s-electron density from the Sn nucleus towards the transition metal. The apparent Sn valency from XAS therefore suggests covalent M–Sn bonding throughout the series with high Sn character.

We examined covalency changes more precisely by determining the ^{119}Sn quadrupole splitting parameter, ΔE_Q, using synchrotron Mössbauer spectroscopy (SMS) of the ^{119}Sn nucleus. The SMS data at 60 K are shown in Fig. 5b with fits to the data yielding ΔE_Q values of 0.623(3), 1.198(2), 1.204(4), 1.134(2), and 0.896(2) mm s^{-1} for complexes **3, 4, 5, 6,** and **7**, respectively. We find a linear correlation of the ^{119}Sn ΔE_Q values here with the Pauling electronegativities of the transition metal (shown in Fig. S10†) where higher electronegativities engender larger ΔE_Q values. This trend can be extended towards formally tetravalent Ph$_3$SnX species (X = I, Br, Cl, OH, F) indicating the ΔE_Q values correlate with the polarity of the axial bond to Ph$_3$Sn. We interpret this trend in our bimetallic series as a change in the M–Sn bond polarity with electron density shifting towards M in more electronegative transition metals.

To complement the spectroscopic analysis of the bonding interaction, we turned to theoretical calculations (details in ESI†). We employed both density functional theory (DFT) and complete active space self-consistent field calculations with corrections from second-order perturbation theory (CASSCF/CASPT2) to analyse the bonding in the ground state. The Mayer bond orders (MBOs) from DFT and CASSCF (Table S14†) both confirm a single M–Sn bond with **7** having the strongest bond (MBO of ∼0.8 in **7** versus ∼0.6 for **3–6**) corroborating analysis of the Raman spectra. Hirshfeld charge decomposition analysis (Tables S17 and S18†) of the sigma bond, which divides the atomic contribution of each element towards a molecular orbital (MO), corroborates that the bond is a polar-covalent interaction with a majority of Sn character. Furthermore, the decomposition agrees with the ^{119}Sn ΔE_Q values where the ratio of % atomic contribution (M : Sn) to the bond changes from 0.57 in **3** to 0.75 in **6**. The X-ray spectroscopy and CASSCF calculations both support a polar-covalent metal–metal interaction which is more polar with less electronegative transition metals.

Computational investigation of the d-based orbitals in **3–6** corroborate a lack of Sn character despite the covalent bond. The calculations confirm the ground states of complexes **3–6** in accordance with the magnetometry, EPR, and electronic absorption data; some of the natural orbitals for **3** are shown in Fig. 6 for illustration. The calculated D values (Table S20†) and electronic excited states (Table S21†) agree with the experimental magnetic data and absorption spectra supporting an accurate description of the electronic structure. Close
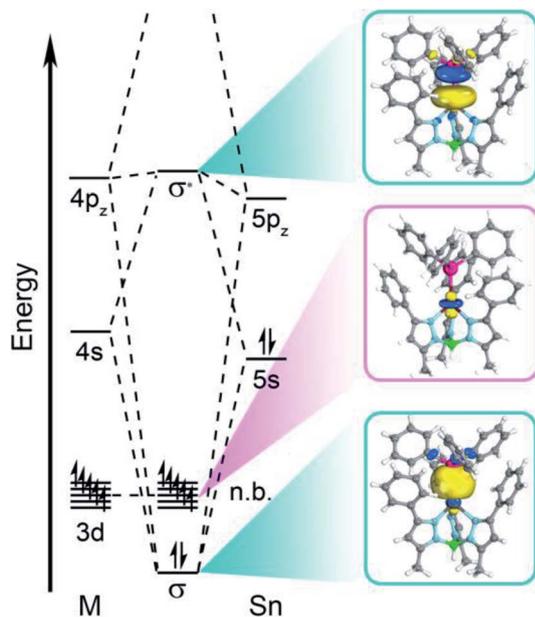
Fig. 6 Qualitative molecular orbital diagram depicting the natural orbitals of the σ-bonding and -antibonding orbitals and the orbital with primarily $3d_{z^2}$ orbital character for compound **3**.

inspection of the natural orbital with $3d_{z^2}$ character reveals the weak ligand field is attributable to a lack of M–Sn antibonding character. This analysis demonstrates that we cannot treat Sn as a ligand in a traditional sense, since the d-orbitals do not mix appreciably with the Sn orbitals. This is best illustrated by Hirshfeld charge decomposition analysis of the frontier molecular orbitals where the $3d_{z^2}$ orbital has ∼2.4% average Sn character for **3–6**. Interestingly, the 4d orbitals have much more Sn character where the $4d_{z^2}$ orbital has ∼11.7% average Sn contribution. The MOs with M–Sn antibonding character are much higher in energy as evidenced by natural orbital occupation numbers (Fig. S11–S14†). Therefore, the 3d orbitals are essentially localized on the transition metal and non-bonding with respect to Sn in **3–6**.

The aggregate data here allow us to construct a qualitative MO picture (shown in Fig. 6) which describes the M–Sn bonding interaction. A foundational aspect of ligand field theory towards describing metal–ligand interactions is the introduction of covalency which implies d orbital-based MOs have metal–ligand antibonding character. Indeed, crystallographic, spectroscopic, and theoretical data show that the Sn donor forms a polar-covalent bond in which electron density shifts away from Sn with more electronegative transition metals. However, we find that the 3d-based MOs have no M–Sn antibonding character, countering the classical MO description of coordination complexes. Consequently, the electronic and magnetic properties in **3–6** are more like a free ion description with respect to the M 3d orbitals despite the covalent M–Sn interaction. This is surprising as the Sn $5s/5p_z$ and M $3d_{z^2}$ orbitals have appropriate symmetry and orbital overlap to form a bonding interaction. We posit that the origin for this observation is energetic mismatch between the M 3d orbitals and the electropositive Sn donor

orbitals. The Hirshfeld charge decomposition analysis supports this as the higher lying M 4s, 4p, and 4d orbitals have more atomic Sn contribution than the 3d-based MOs. This suggests that the localization of the M 3d orbitals are due to the higher energy of the Ph_3Sn donor orbitals relative to the 3d orbitals. This energetic mismatch is supported by atomic ionization potentials and energies of the hydrogen-like atomic orbitals.[55]

Conclusions

The comprehensive study reported herein illuminates the importance of energetic alignment in governing orbital interactions and spin ground states. Specifically, the better alignment of Sn donor orbitals with transition metal 4s and 4p orbitals yield highly localized, non-bonding 3d orbitals. This engenders a weak ligand field about the transition metal stabilizing a high-spin ground state, unusual to bimetallic complexes. Understanding such factors governing metal–metal interactions will be crucial in cooperative catalysis and targeting spin-selective reactivity. This demonstrates the potential use of electropositive main group metals in stabilizing unusual electronic structures. Furthermore, the bonding analysis here represents an advancement in the fundamental understanding of metal–metal interactions, particularly with Sn which has been proposed to promote inverted ligand fields.[56]

Conflicts of interest

There are no conflicts to declare.

Acknowledgements

Notes and references

1 O. Kahn, *Molecular Magnetism*, VCH, Weinheim, Germany, 1993.

2 D. Danovich and S. Shaik, *J. Am. Chem. Soc.*, 1997, **119**, 1773–1786.

3 D. Schröder, S. Shaik and H. Schwarz, *Acc. Chem. Res.*, 2000, **33**, 139–145.

4 R. Poli and J. N. Harvey, *Chem. Soc. Rev.*, 2003, **32**, 1–8.

5 S. M. Bellows, T. R. Cundari and P. L. Holland, *Organometallics*, 2013, **32**, 4741–4751.

6 B. N. Figgis and M. A. Hitchman, *Ligand Field Theory and Its Applications*, Wiley-VCH, New York, 2000.

7 J. A. Chipman and J. F. Berry, *Chem. Rev.*, 2020, **120**, 2409–2447.

8 G. Aullón and S. Alvarez, *Theor. Chem. Acc.*, 2009, **123**, 67–73.

9 M. S. Holt, W. L. Wilson and J. H. Nelson, *Chem. Rev.*, 1989, **89**, 11–49.

10 A. Weickgenannt and M. Oestreich, *Chem.–Eur. J.*, 2010, **16**, 402–412.

11 D. Das, S. S. Mohapatra and S. Roy, *Chem. Soc. Rev.*, 2015, **44**, 3666–3690.

12 P. Buchwalter, J. Rose and P. Braunstein, *Chem. Rev.*, 2015, **115**, 28–126.

13 M. Pereyre, J. P. Quintard and A. Rahm, *Tin in Organic Synthesis*, Butterworth, London, 1987.

14 Y. Cao, J. L. Peterson and A. L. Stolzenberg, *Inorg. Chem.*, 1998, **37**, 5173–5179.

15 N. D. Smith, J. Mancuso and M. Lautens, *Chem. Rev.*, 2000, **100**, 3257–3282.

16 Z. Wang, Z. Yao, Z. Lyu, Q. Xiong, B. Wang and X. Fu, *Chem. Sci.*, 2018, **9**, 4999–5007.

17 A. McSkimming and W. H. Harman, *J. Am. Chem. Soc.*, 2015, **137**, 8940–8943.

18 K. Uehara, S. Hikichi and M. Akita, *J. Chem. Soc., Dalton Trans.*, 2002, 3529–3538.

19 S. C. Coste, T. J. Pearson and D. E. Freedman, *Inorg. Chem.*, 2019, **58**, 11893–11902.

20 B. Cordero, V. Gómez, A. E. Platero-Prats, M. Revés, J. Echeverría, E. Cremades, F. Barragán and S. Alvarez, *Dalton Trans.*, 2008, 2832–2838.

21 F. A. Cotton, C. A. Murillo and R. A. Walton, *Multiple Bonds Between Metal Atoms*, Springer, New York, 2005.

22 B. Kamb and L. A. Pauling, *Proc. Natl. Acad. Sci. U. S. A.*, 1986, **83**, 3569–3571.

23 W. Petz, *Chem. Rev.*, 1986, **86**, 1019–1047.

24 M. F. Lappert and R. S. Rowe, *Coord. Chem. Rev.*, 1990, **100**, 267–292.

25 S. J. Tereniak, R. K. Carlson, L. J. Clouston, V. G. Young Jr, E. Bill, R. Maurice, Y.-S. Chen, H. J. Kim, L. Gagliardi and C. C. Lu, *J. Am. Chem. Soc.*, 2014, **136**, 1842–1855.

26 R. J. Eisenhart, R. K. Carlson, L. J. Clouston, V. G. Young Jr, Y.-S. Chen, E. Bill, L. Gagliardi and C. C. Lu, *Inorg. Chem.*, 2015, **54**, 11330–11338.

27 R. J. Eisenhart, L. J. Clouston and C. C. Lu, *Acc. Chem. Res.*, 2015, **48**, 2885–2894.

28 A. Vogler and H. Kunkely, *J. Organomet. Chem.*, 1988, **355**, 1–6.

29 A. B. P. Lever, *Inorganic Electronic Spectroscopy*, Elsevier Science Publishers B. V., Amsterdam, 1984.

30 J. Krzystek, D. C. Swenson, S. A. Zvyagin, D. Smirnov, A. Ozarowski and J. Telser, *J. Am. Chem. Soc.*, 2010, **132**, 5241–5253.

31 J. J. Scepaniak, T. D. Harris, C. S. Vogel, J. Sutter, K. Meyer and J. M. Smith, *J. Am. Chem. Soc.*, 2011, **133**, 3824–3827.

32 S. E. Creutz and J. C. Peters, *Inorg. Chem.*, 2016, **55**, 3894–3906.

33 W. A. G. Graham, *Inorg. Chem.*, 1968, **7**, 315–321.

34 H. Kameo, S. Ishii and H. Nakazawa, *Organometallics*, 2012, **31**, 2212–2218.

35 S. Aldridge, *Angew. Chem., Int. Ed.*, 2008, **47**, 2348–2350.

36 M. A. Fox, T. B. Marder and L. Wesemann, *Can. J. Chem.*, 2009, **87**, 63–71.

37 S. Ye and F. Neese, *J. Chem. Theory Comput.*, 2012, **8**, 2344–2351.

38 R. T. Azuah, L. R. Kneller, Y. Qiu, P. L. W. Tregenna-Piggott, C. M. Brown, J. R. D. Copley and R. M. Dimeo, *J. Res. Natl. Inst. Stand. Technol.*, 2009, **114**, 341–358.

39 P. J. Desrochers, J. Telser, S. A. Zvyagin, A. Ozarowski, J. Krzystek and D. A. Vivic, *Inorg. Chem.*, 2006, **45**, 8930–8941.

40 M. J. Rose, D. E. Bellone, A. J. Di Bilio and H. B. Gray, *Dalton Trans.*, 2012, **41**, 11788–11797.

41 J. Krzystek, A. Ozarowski, S. A. Zvyagin and J. Telser, *Inorg. Chem.*, 2012, **51**, 4954–4964.

42 D. E. Freedman, W. H. Harman, T. D. Harris, G. J. Long, C. J. Chang and J. R. Long, *J. Am. Chem. Soc.*, 2010, **132**, 1224–1225.

43 W. H. Harman, T. D. Harris, D. E. Freedman, H. Fong, A. Chang, J. D. Rinehart, A. Ozarowski, M. T. Sougrati, F. Grandjean, G. J. Long, J. R. Long and C. J. Chang, *J. Am. Chem. Soc.*, 2010, **132**, 18115–18126.

44 D. Pinkowicz, F. J. Birk, M. Magott, K. Schulte and K. R. Dunbar, *Chem.–Eur. J.*, 2017, **23**, 3548–3552.

45 C. V. Popescu, M. T. Mock, S. A. Stoian, W. G. Dougherty, G. P. A. Yap and C. G. Riordan, *Inorg. Chem.*, 2009, **48**, 8317–8324.

46 S. Stoll and A. Schweiger, *J. Magn. Reson.*, 2006, **178**, 42–55.

47 C. Duboc, T. Phoeung, S. Zein, J. Pécaut, M.-N. Collomb and F. Neese, *Inorg. Chem.*, 2007, **46**, 4905–4916.

48 C. Duboc, *Chem. Soc. Rev.*, 2016, **45**, 5834–5847.

49 V. K. Jain and G. Lehmann, *Phys. Status Solidi B*, 1990, **159**, 495–544.

50 V. Y. Lee and A. Sekiguchi, *Organometallic Compounds of Low-Coordinate Si, Ge, Sn, and Pb*, John Wiley and Sons, West Sussex, UK, 2010.

51 F. Farges, R. L. Linnen and G. E. Brown Jr, *Can. Mineral.*, 2006, **44**, 795–810.

52 E. R. Aluri and A. P. Grosvenor, *Phys. Chem. Chem. Phys.*, 2013, **15**, 10477–10486.

53 H.-T. Wang, M. K. Srivastava, C.-C. Wu, S.-H. Hsieh, Y.-F. Wang, Y.-C. Shao, Y.-H. Liang, C.-H. Du, J.-W. Chiou, C.-M. Cheng, J.-L. Chen, C.-W. Pao, J.-F. Lee, C. N. Kuo, C. S. Lue, M.-K. Wu and W.-F. Pong, *Sci. Rep.*, 2017, 7, 40886.

54 H. Masai, T. Ina, S. Okumura and K. Mibu, *Sci. Rep.*, 2018, **8**, 415.

55 C. E. Moore, *Ionization Potentials and Limits Derived from the Analyses of Optical Spectra NSRDS-NBS 34*, National Bureau of Standards, 1970, Washington DC.

56 R. Hoffmann, S. Alvarez, C. Mealli, A. Falceto, T. J. Cahill, T. Zeng and G. Manca, *Chem. Rev.*, 2016, **116**, 8173–8192.